Magnon profile on $SrRuO_3$ films studied by inelastic neutron scattering

G. D. Dwivedi,[1,*] C.-M. Wu,[2,*] Bo-Yu Chen,[1] S. T. Lin,[1] W.-Z. Qiu,[1] S. J. Sun,[3,1,†] Guangyong Xu,[4] J. W. Lynn,[4] J. W. Chiou,[3] C.-H Lee,[5] W.-H. Li,[5] S. Yano,[2] and H. Chou[1,3,†]

[1]*Department of Physics, National Sun Yat-sen University, Kaohsiung, Taiwan, 80424, R.O.C.*
[2]*National Synchrotron Radiation Research Center, Hsinchu, Taiwan, 30076, R.O.C. and Australian Nuclear Science and Technology Organization, New South Wales, Australia*
[3]*Department of Applied Physics, National University of Kaohsiung, Kaohsiung, Taiwan, R.O.C.*
[4]*NIST Center for Neutron Research, National Institute of Standards and Technology, Gaithersburg, Maryland 20899, USA*
[5]*Department of Physics, National Central University, Taoyuan City, Taiwan, R.O.C.*

(Received 23 May 2019; revised manuscript received 11 January 2020; accepted 15 January 2020; published 3 February 2020)

In this study, the inelastic neutron scattering probe of SIKA in ANSTO is employed to investigate the magnon dispersion curve in ferromagnetic $SrRuO_3$ single crystal epitaxial films and to better understand the underlying mechanisms. This report presents the successful measurement of a magnon peak from the $SrRuO_3$ films which contained an amount of material of only 0.9 mg. We reveal one significant magnon dispersion curve along [002] following the quadratic ($E \propto Q^2$) relation, which shows a magnon gap of 0.32 meV. We have discussed several possible mechanisms, such as the higher symmetry structure and the impurity levels, which may contribute to this smaller gap.

DOI: 10.1103/PhysRevB.101.054403

I. INTRODUCTION

$SrRuO_3$ is a rare 4*d* ferromagnetic material with ferromagnetic and metal-metal transition around the Curie temperature (T_C) 165 K [1–9]. Due to this itinerant ferromagnetic behavior $SrRuO_3$ is widely used as a conductive electrode in many oxide multilayer device applications [10–23]. Even though $SrRuO_3$ is a widely known and well-studied material, a few questions remain unanswered, such as the unsaturated magnetization at high magnetic field, the unbelievably high upper-limit temperature ($T \leqslant 30$ K) for Fermi liquid conduction, the role of magnons in the non-Fermi-liquid behavior within $90\,\mathrm{K} \leqslant T \leqslant 150\,\mathrm{K}$, the source of magnon gap and the mechanism of carrier-type change i.e., hole-conduction at room temperature and electron-conduction at low temperature. These puzzles, as depicted by Koster *et al.* [24] are believed to associate strongly with the degree of correlation within the carriers as well as the O2*p* and Ru4*d* bands. Recently, the non-Fermi-liquid behavior of $SrRuO_3$ within the range of $90\,\mathrm{K} \sim T_C$ is found to govern by magnons via electron-magnon coupling [25]. This result does not follow the conventional understanding because typically electron-phonon coupling dominates at such high temperatures. This finding indicates that magnon is not an independent factor along with others. A similarly spectacular phenomenon was observed in Hall measurement, a sign change in Hall coefficient shows the conduction carrier changes from a hole-type at high temperature to an electron-type at low temperature [26,27]. A simple two-bands model, which is either formed by an overlapping of the conduction and valence bands at different *k* directions or a crossing or an anticrossing, cannot explain the change of carrier type. The structural change, due to the strain effect at film/substrate interface and the massive Ru and O vacancies, may alter the electrons and magnons behavior and the correlation between them via many interaction routes and contribute to this exciting phenomena. To solve these underlying physics, we need to understand the ground state properties of magnons, and the dispersion relation of magnon which could be studied by the inelastic neutron scattering (INS).

INS is a very powerful tool for probing low-energy excitation quasiparticles such as magnons and phonons. But, due to the extremely small inelastic scattering cross section, it requires a large amount of specimen. In 2016, Itoh *et al.* [28] employed the INS measurement on a sizeable polycrystalline sample of 73 g by a time of flight technique to investigate the magnon profile. They discovered a 2-meV magnon gap in $SrRuO_3$ polycrystal and they attributed this gap opening to Weyl fermions. Recently, Jenni *et al.* observed a magnon gap of 1 meV in 6 g of $SrRuO_3$ single crystals by INS measurements and they also attributed the role of Weyl fermions in magnon gap opening [29]. Due to the requirement of vast amount of specimen material, it is rare and even impractical to use film samples to study INS experiments even though thin films are the most feasible format for modern applications. Until now, only one report related to INS on a thick multilayer film sample over 1 μm is available [30].

Fortunately, neutron facilities have been greatly improved in recent years, so it is possible now to investigate the low energy excitation on films by the INS technique. In this study, we chose $SrRuO_3$ single crystal epitaxial films as the specimen material and used the powerful INS function of SIKA in ANSTO to measure the dispersion curve of magnons along

*These authors contributed equally to this paper.
†Corresponding authors: sjs@nuk.edu.tw; hchou@mail.nsysu.edu.tw

a specific direction, which exhibits enormous contribution of magnetic signal. A magnon dispersion curve along the [002] direction has been successfully observed and an estimated reduced magnon gap of 0.32 meV was found for $SrRuO_3$ single crystal epitaxial films, which is one third of that observed by Jenni *et al.* [29] and almost one sixth of the observation of Itoh *et al.* [28]. The major difference between their $SrRuO_3$ systems and our film system is the crystal structure and the Ru and O vacancy concentrations. Polycrystalline bulk and single crystal system both are orthorhombic, while our film system exhibits near cubic structure. The film systems were found to have significant Ru and oxygen vacancies similar to earlier reports [31,32], while the single crystal [29] and the polycrystalline samples [28] have $T_C = 165$ K and should have negligible vacancies according to Dabrowski's report [9]. Moreover, the $SrRuO_3$ polycrystalline system has reportedly exhibited Ru deficiency when mixed in a stoichiometric weight ratio and it has been shown that Ru-vacancies modify the properties significantly [33]. The vacancies are an integral part of $SrRuO_3$ film system and it plays a very pivotal role in determining the properties of film systems. The smaller magnon gap observed in our film could be strongly associated with two factors: (1) the near cubic crystal structure indicates a higher order of symmetry and (2) the impurity level due to massive Ru and O vacancies. The impurity level and the higher symmetry disrupt the formation of anticrossings, which could lead to two different scenarios: (i) it could weaken Weyl Fermion, which in turn weakens the spin-orbit coupling. In this case the on-site Coulomb repulsion may or may not participate in interfering with the spin-orbit coupling. (ii) The impurity level and the higher symmetry could destroy Weyl Fermions and then the impurity level induced strong on-site Coulomb repulsion could give rise to a small magnon gap.

II. EXPERIMENT

The four $1 \times 1\,cm^2$ $SrRuO_3$ single crystal epitaxial films with a thickness of 260 nm and a total mass of $\sim$0.9 mg were grown by the standard laser ablation technique. INS measurements on single crystal films were conducted at ANSTO, using the cold-neutron triple-axis spectrometer SIKA with the energy of neutrons defined by double-focusing pyrolytic graphite (PG) (002) crystals at the monochromator position and vertical focusing PG(002) crystals at the analyzer position, using a fixed final energy of 8.07 meV with a 5-cm-thick PG filter to suppress higher order contaminations. To optimize the signal to noise ratio for the INS measurements, a narrow beam of $50 \times 50\,mm^2$ limited by an aperture placed behind the sapphire filter was used and the sample was masked with a B_4C neutron absorber. This configuration gives an energy resolution of $\sim$0.29 meV and a background signal of 0.7 count per minute for the measurement on SIKA. Initial INS measurements were also perfomred at NIST, employing the spin polarized inelastic neutron spectrometer (SPINS), operated in its conventional triple axis mode, with the energy of neutrons defined by PG(002) monochrometor crystals and PG(002) analyzer crystals, a collimation of 80′ for the in-pile beam and 80′-open before and after the sample positions, and a Be filter at 77 K to suppress higher order contaminations. This configuration with a final energy of 5 meV gives an energy resolution of $\sim$0.2 meV. The temperature was controlled with the AS Scientific top loading cryofurnace operated between 5 and 200 K. The room temperature electronic state of $SrRuO_3$ was examined by x-ray photoemission spectroscopy (XPS). Both the films and a reference bulk were performed using a Thermo Scientific ESCALAB 250 system operating at an average base pressure of $\sim 6 \times 10^{-9}$ torr (1 torr = 133.3 Pa) with a monochromatic MgK_α line at 1256 eV and with a total energy resolution of about 0.02 eV. In addition to the depth profile, photoemission spectra were measured after removing the sample surfaces by sputtering, and only the material deep at the center of the film or inside the bulk were measured.

III. RESULTS AND DISCUSSION

$SrRuO_3$ epitaxial films have been grown on single crystalline $SrTiO_3$ (001) substrates for inelastic neutron scattering experiments. Figure 1(a) shows a x-ray diffraction (XRD) pattern of $SrRuO_3/SrTiO_3$(002) peaks indicating an epitaxially grown structure. Lattice constants (c) of $SrRuO_3$ film and $SrTiO_3$ substrate calculated from their (002) peaks are approximately 3.96 and 3.905 Å. The resistance as a function of temperature measurement of $SrRuO_3$ films grown on $SrTiO_3$ (001) planes exhibit T_C around 152 K, indicating the excellent quality of the film [Fig. 1(b)]. To produce the reciprocal space mapping of the SRO/STO system we searched for the (103) plane of the system. The XRD reciprocal space mapping of SRO (103) and STO (103) peaks is shown in Fig. 1(c), where the lattice constants of SRO film are calculated to be $a = 3.968$ Å and $c = 3.920$ Å. The φ scan of SRO (103) peak, Fig. 1(d), exhibits four-poles fold symmetry confirming the epitaxial growth of the SRO film on the STO substrate with very high quality. The room temperature crystal structure of the $SrRuO_3$ films is modified by the interfacial strain and Ru and O vacancies to transform from the orthorhombic bulk ($a = 5.57$ Å, $b = 5.53$ Å, and $c = 7.85$ Å) to the tetragonal film ($a = b = 3.968$ Å and $c = 3.920$ Å). The samples were slowly cooled down to 5 K with few intermediate steps for instrumental calibrations and lattice constant measurements with neutron diffraction at 200 and 5 K along (0,−1,0), (0,−2,0), (0,−2,2), and (0,0,2). The lattice of $SrRuO_3$ shrinks to a cubic one with $a = b = c = 3.9159$ Å at 200 K and further to a tetragonal one with $a = b = 3.8915$ Å, $c = 3.8973$ Å at 5 K. The equal shrinkage of the in-plane lattices can be attributed to the interface effect. The change in the c axis is interesting, as it has suppressed only slightly from room temperature to 200 K while in-plane suppression is quite significant. This could be explained as following; the large in-plane contraction exerts a force perpendicular to the ab plane (i.e., along the c axis) and tries to expand the c axis, which compensates the shrinking due to lowering temperature. At 5 K, the shrinkage on lattice constants due to lowering temperature wins out the expansion in the c axis because of the in-plane contraction results in a small c axis. The total shrinkages of axes from 5 K to room temperature are −1.9% and −0.57% along the a-b axes and c axis. The tetragonal structure has a shorter c axis at room temperature and becomes a slightly longer one at 5 K. The strain in the film system could be calculated from $\varepsilon = 2(c - a)/(c + a)$. The strain

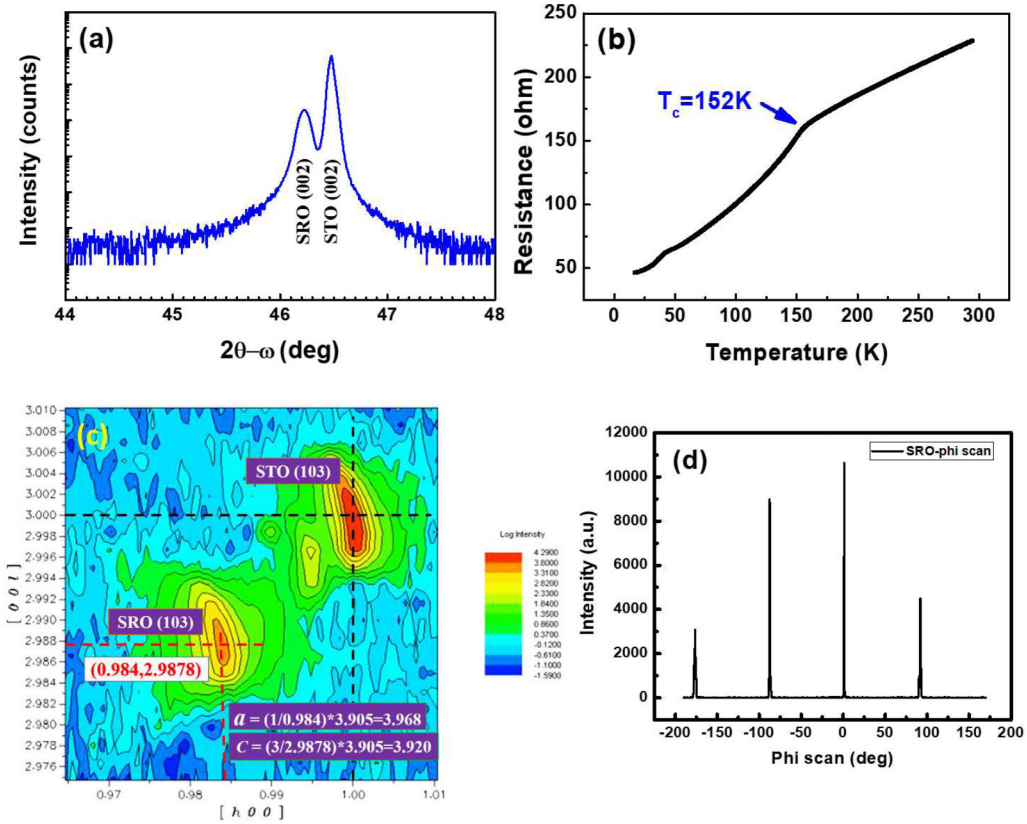

FIG. 1. (a) X-ray diffraction pattern of a $SrRuO_3$ film deposited on a $SrTiO_3$ (001) plane. (b) Resistance versus temperature measurement of film provides metal to metal transition (which corresponds to ferromagnetic transition) around 150 K. (c) X-ray reciprocal space mapping of SRO/STO(103) plane and (d) the phi scan of SRO (103) peak of (c).

developed in the film system at 300 K is 12×10^{-3} and at 5 K is about 1.5×10^{-3}. In polycrystalline bulk $SrRuO_3$ the developed strain along *a-c* plane is 6.84×10^{-3} and along the *b* axis is 4.74×10^{-4} at 300 K, while it is 6.36×10^{-3} along *a-c* plane and 2.81×10^{-4} along the *b* axis at 10 K. It is obvious that the interfacial strain along with Ru and O vacancies [31,32,34] changes the crystal structure more symmetrically. The crystal structure and crystal symmetry of the present film is very different from Jenni's single crystal and Itoh's polycrystalline samples which are orthorhombic.

A series of spectra were taken along [00*L*] direction with $L \leqslant 1.9$ to minimize the influence of the (002) Bragg peaks of both STO and SRO. Itoh *et al.* [28] observed magnon peaks in $SrRuO_3$ polycrystals below the ferromagnetic transition temperature at several Q values such as 0.2, 0.25, and 0.3 $Å^{-1}$ with full width at half maximum (FWHM) around 2.5 meV. They calculated the ferromagnetic spin wave gap of 2 meV and magnon stiffness ~62. Jenni *et al.* [29] used $SrRuO_3$ single crystals to measure several energy scans across the magnon dispersion at 10 K. They observed a magnon gap of 1 meV and magnon stiffness ~87. They have studied temperature dependence of magnon gap and stiffness and according to their report the magnon gap and stiffness of polycrystalline $SrRuO_3$ [28] is proportional to magnetization curve $M(T)$, while a magnon gap and stiffness of single crystal $SrRuO_3$ [29] do not follow the $M(T)$ curve. The optical Hall conductivity in the tetrahertz region had confirmed the existence of Weyl fermions within the 5-meV range of the Fermi level [35]. Single crystal and polycrystalline $SrRuO_3$ possess room temperature orthorhombic crystal structure that leads to a considerable anisotropy. Obviously, the interface effect makes the in-plane and out-of-plane lattice constants of the present films nearly the same. The near cubic structure of the present films exhibit higher isotropy and smaller octahedral distortion, hence we expect the present films should exhibit a smaller magnon gap at 5 K and the magnons at various Q values might shift to lower energy regions. In this study, we selected three L values such as 1.9, 1.8, and 1.7, which are equivalent to $Q = 1.53$ $Å^{-1}$, $Q = 1.45$ $Å^{-1}$, and $Q = 1.37$ $Å^{-1}$, respectively, to scan the INS. According to SIKA's configuration, we choose $E_f = 8.07$ meV to be the end energy, E_f, which provides a reasonable energy resolution of 0.298 meV and wider maneuverability in Q value and energy spans.

The most crucial scan for $Q = 1.53$ $Å^{-1}$, as it is the closest one to the zone center and should have strongest and narrowest magnon peak, we scanned four times from −0.7 to 2.3 meV with step sizes of 0.1 or 0.15 meV to ensure the reliability of the data. The collection time for each data point was 15 min. Each scan shows an evident peak around 0.7 meV indicating the observed peaks are not fake ones due to other effects. The averaged data curve for $Q = 1.53$ $Å^{-1}$ is plotted in Fig. 2(a). The small error bars, with the size very similar to the size of data points, indicates a very high accuracy measurement of this curve. The target peak is found to locate at 0.7 meV with a relatively narrow FWHM of ~0.31 meV. Figures 2(b) and 2(c) present quick energy scans for $Q = 1.45$

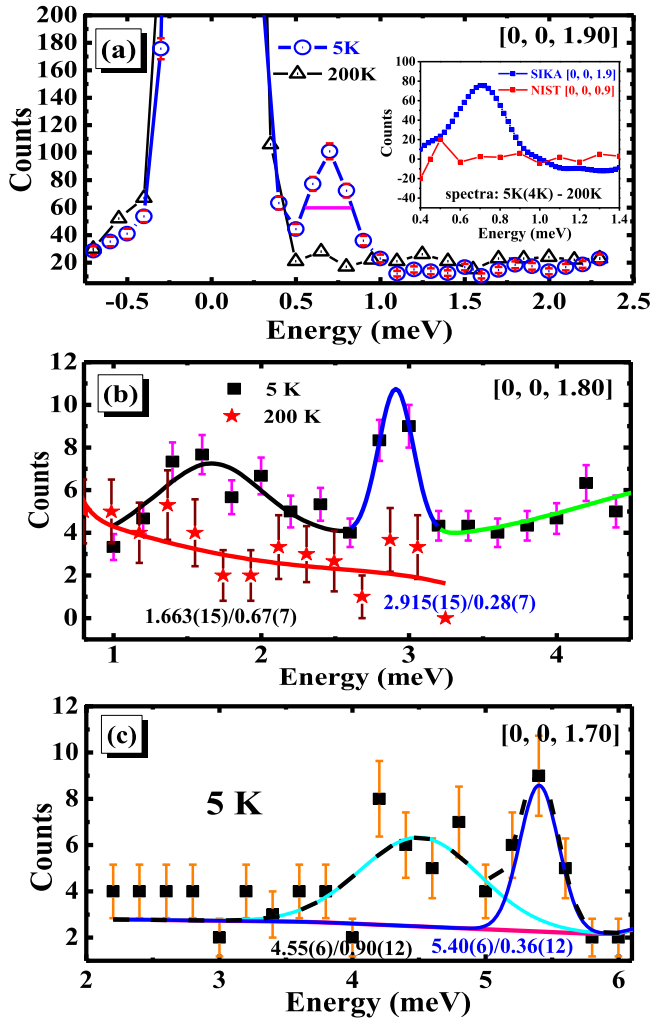

FIG. 2. (a) The INS spectra of $L = 1.90$ at 5 and 200 K. The horizontal bar (color: magenta) is the energy resolution. Inset of (a) show residuals of INS scans taken at low temperature (4 and 5 K) and high temperature (200 K) along [0, 0, 0.90] and along [0, 0, 1.90]. (b) INS measurement along the [0, 0, 1.80] direction at 5 K (solid black squares) and 200 K (solid red stars). Broad magnon peak arising from high-defect region is fitted with solid black line, while narrow magnon peak arising from low-defect region is fitted with solid blue lines. Red line is fitting line of INS data measured at 200 K. (c) INS along [0, 0, 1.70] direction at 5 K. The black and blue numbers are the magnon peak positions/FWHM of various Q values. The error is calculated by taking square-root of data points. Uncertainties represent one standard deviation.

and 1.37 $Å^{-1}$, respectively. The large error bars are the result of short scan time. After comparing with the energy scan of $Q = 1.53$ $Å^{-1}$, we found each plot has a peak with similar FWHM and is fitted with blue curves. These peak positions and FWHM increases with Q value, which follow the original expectation. Another small broad peak-like structure located at energy lower than magnon peaks cannot be explained by the phonons of $SrRuO_3$ [36] or $SrTiO_3$ [37] as they locate at higher energy region and should exhibit nearly linear energy dependence. A reasonable explanation for the appearance of both narrow and broad peaks is the nonuniform distribution of defects. The low defect density region attributed to the narrow peak, while the high defect density parts reduces the coupling strength that reduces the excitation energy, less than 1 meV in $Q = 1.45$ $Å^{-1}$ and 1.37 $Å^{-1}$, and lifetime producing broad peaks. More experiments are needed to clarify the exact origin of the broad peaks.

To confirm that the observed peak is contributed by the magnon and not by phonons or instrumental errors, it is necessary to take another scan at a high temperature where the material is in a paramagnetic state. If the peak intensity disappears or enhances or remains unchanged, then it is reasonable to consider that the peak is attributed by magnon, phonon, or instrumentation, respectively. The center peaks in Fig. 2(a) at 0 meV overlap perfectly while the peak around 0.7 meV at 5 K clearly disappears at 200 K. One may argue that these peaks could be due to the tail of the main lattice peak of the substrate and the change in intensities at 5 and 200 K were due to the phase transition of the substrate around 105 K. Since the lattice parameters of the substrate are smaller than that of the film in all the temperature region, therefore, the Bragg peak of the substrate should locate at a higher Q value than the film. In the present case we measured the energy dispersion towards lower Q values and the magnon peaks are clearly separated with the tail of the Bragg peak of the films, hence we can confidently say that these peaks are not due to the tail of the main peak of the substrate. The disappearance of the peak at around 0.7 meV at 200 K proves that the observed peak is a magnon peak. Similar results along [0, 0, 1.8] in Fig. 2(b), even with quick scans, both the sharp and the broad peaks, around 2.9(2) and 1.6(5) meV at 5 K disappear at 200 K. This proves that both peaks are magnon peaks. Since the magnon dispersion curve close to the zone center can be described by a quadratic equation, the dispersion curve for the broad peak along [0,0,1.9] can be estimated to locate at around $0.4 \sim 0.5$ meV, which is at the valley sandwiched by the tail of the Bragg peak and the sharp magnon peak. The broad peaks along [0,0,1.8] and [0,0,1.7] have intensities around half of the sharp one, therefore the intensity of the broad peak along [0,0,1.9] follows the same trend as it has an intensity similar to the background that makes it invisible in the present data. We have successfully challenged the concept that the films with extremely less mass are unable to measure INS.

Interestingly, the magnon peak was not observed along the [001] direction for both the SIKA of ANSTO and the initial SPINS of NIST. To reveal the possible magnon peak, the low temperature spectra are subtracted by the high temperature one, as shown in the inset of Fig. 2(a) along [0, 0, 1.9] and along [0, 0, 0.9]. The residual along [0, 0, 0.19] is exactly the magnon peak observed at 5 K, while that along [0, 0, 0.9] is only a line of noise. We were unsuccessful to observe any magnon peaks along [0, 0, 0.9]. The reason for this difficulty could be understood as the crystal structure factor of (001) plane for $SrRuO_3$ is much smaller than crystal structure factor of (002) (by a factor of >50) with or without magnetic contributions before and after the crystal phase transition. In addition to the small mass of the present epitaxial single crystal films, we could not observe the magnon peak along [0, 0, 0.9] for the films.

Using the present identified magnon peaks, we plotted a dispersion curve in Fig. 3(a). The red dots are the data measured by Itoh's group from powder inelastic diffraction

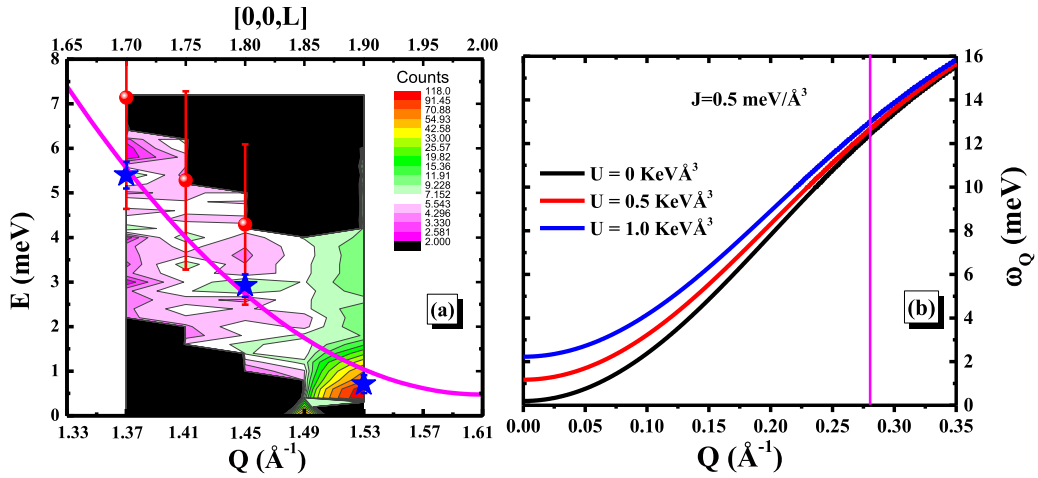

FIG. 3. (a) Relationship between E and L (or Q). Data points presented as blue stars are the position of magnon peaks as obtained from the Fig. 2. These magnon peaks follow the dispersion relationship ($E \propto Q^2$). The data points presented as red circles are obtained from Ref. [28]. The center of magnon peaks have been depicted as red circles and the red bars represents the FWHM of magnon peaks. The data points obtained from our measurements matches well with Ref. [28] and are situated well within their FWHM. (b) The magnon dispersions in different Coulomb U at temperature $T = 0$. The magnetic coupling $J = 0.5\,\text{meV Å}^{-3}$, the conduction-band electron density $n_e = 1 \times 10^{-4}\,\text{Å}^{-3}$ and the Ru occupation $c_{\text{Ru}} = 10^{-3}\,\text{Å}^{-3}$.

and the vertical lines on each red dot are the FWHM of their peaks. The blue stars are the data point of the present study. The FWHM of each point is around $0.2 \sim 0.3$ meV. A quadratic equation can approximate the present magnon dispersion relationship between energy (E) and wave vector (Q) [38]

$$E = \hbar\omega = A + BQ^2,$$

where, A and B are constants and represent magnon gap and magnon stiffness, respectively. For the present case, these two factors as described in the previous paragraph must give a different magnon dispersion curve to Heisenberg model. However, near the zone boundary, the dispersion curve can still be reasonably approximated and estimated by the Heisenberg model. Fitting the data points with the above dispersion relation, we obtained a magnon gap (A) at $Q = 1.6\,\text{Å}^{-1}$ ($L = 2.0$) of 0.32 meV with a standard deviation of 0.36 meV. This magnon band gap of 0.32 meV is much smaller than Itoh's 2 meV [28], Jenni's 1 meV [29], and a ferromagnetic resonance (FMR) measurement of 1 meV [39]. However, assuming a zero gap does not give rise to a good fitting result. It is worth mentioning that the magnon stiffness "B" in the present case is around 22 meV Å^2, which is significantly smaller than the reported values of Itoh *et al.* [28] and Jenni *et al.* [29], indicating films are substantially different from their bulk and single crystal counterparts.

The reduced magnon gap of present $SrRuO_3$ films could be due to three possible reasons: First, the near cubic crystal structures of $SrRuO_3$ films enhance the isotropy of the system as we mentioned above, which may suppress the magnon gap. The second possible factor is the interface effect; due to interface strain or band bending act as an internal field applied to the film. This effect may assist in forming an initial layer with higher symmetry that helps the subsequence growth of the films. However, the interface effect is only effective in few nm range, but our present films have a thickness of 260 nm, hence the interface effect most probably would not affect the whole film. Similarly, the neutron scattering signal is a majorly collective contribution from the whole film. The interface effect has a negligible effect to the inelastic scattering signal and the reduction of the magnon gap. The third possible factor is the expected Ru vacancies along with O vacancies in the samples that may change the Ru electronic state or weaken the spin-orbital coupling or could introduce local on-site Coulomb coupling. The third possibility will be discussed in more detail in the following section.

The composition of films measured by XPS depth profile and electron dispersion spectra measurements (not shown here) suggests a distinct deficiency of Ru and O in the films as other groups also have observed [31,32,34]. According to our previous study [40], we propose a narrow impurity band that could arise from these vacancies located around the Fermi level and successfully explain the unique phenomenon that the conduction carrier of $SrRuO_3$ changes sign from a hole conduction at a higher temperature to an electron conduction at a low temperature. The existing impurity band can be confirmed from the cumulative plot of the valence band spectra ($-1.5 \sim 3$ eV) of $SrRuO_3$ single crystal epitaxial films, as shown in Fig. 4, which is composed of Ru4$d(t_{2g})$–O2p hybridized states and can be simulated by two Ru4$d(t_{2g})$ peaks and one O2p peak [40,41]. The XPS intensity of the film is much lower than that of the bulk near the Fermi level. The Fermi level is assumed to locate at the first Ru4$d(t_{2g})$ peak maximum for enabling metallic properties. The XPS intensity of the film extends to a further range above the Fermi energy and all peaks within this energy region are suppressed to smaller values than that of the bulk, which indicates the original band has been modified due to the impurity band that results in a weaker Ru4$d(t_{2g})$–O2p hybridization in the films that led to the observed decrease in T_C (155 K) and higher resistivity. Resultantly, the anticrossings of the original band, which gives rise to Weyl fermions, could be destroyed and the magnon gap observed by Itoh *et al.* [28] and Jenni *et al.* [29] should become smaller or disappear. In another scenario, the

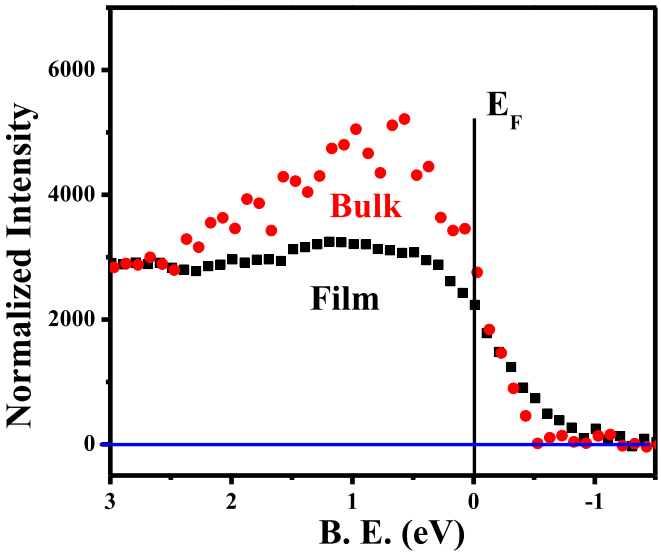

FIG. 4. X-ray photoemission spectra of valence band regions of $SrRuO_3$ film (black solid square) and $SrRuO_3$ bulk (red solid circle).

Ru and O vacancy states could capture electrons that gives rise to a strong e-magnon coupling [25] and is responsible for the carrier sign change phenomenon [40], and could induce strong on-site Coulomb interactions between these captured electrons. In order to investigate the band gap opening, we proposed a magnetic Hamiltonian to calculate the magnon dispersion.

The Hamiltonian of $SrRuO_3$ can be written as

$$H = H_0 + H_J + H_U. \tag{1}$$

The first term, H_0, describes the conducting carriers itinerating in the conducting bands. In our calculations, we limited the temperature to below T_C and the polarity of carriers is *n*-type, i.e., electron-type, as other studies and our experiment results show [26,27,40].

The second term describes the spin interaction between magnetic Ru ions and conduction electrons, which gives rise to the ferromagnetism of $SrRuO_3$, and can be written as

$$H_J = -\int dr c_{Ru} J(r) \vec{S}(r) \cdot \vec{\sigma}(r), \tag{2}$$

in which $J(r)$ is the magnetic coupling between Ru spin $\vec{S}(r)$ and conducting electron's spin $\vec{\sigma}(r)$; c_{Ru} is the density of Ru occupation. For simplicity, $J(r)$ can be approximated to be a constant J.

The third term, the aforementioned Coulomb interactions, could arise from O or Ru vacancies when some electrons were captured by them. It should be noted that although the Coulomb interactions act on the captured electrons, the conduction band of $SrRuO_3$ will feel an effective Coulomb interaction. Therefore, the Hamiltonian H_U can be written in the form

$$H_U = U \int dr n(r)_\uparrow n(r)_\downarrow, \tag{3}$$

in which U is the effective Coulomb constant to the conduction band; $n_\uparrow$ and $n_\downarrow$ are electron carrier densities in the conduction band with different spin indexes, $\uparrow$ and $\downarrow$.

The magnon dispersion, ω_q, is the momentum q-dependent eigenvalue of the spin-spin correlation functions from Ru spins. The spin-spin correlation function or Green's function has the form

$$G_{rr'}(t) = -i\theta(t)\langle [S_r{}^+(t), S_{r'}^-(0)]\rangle, \tag{4}$$

in which t is the time, $\theta(t)$ is the step function and S_r^+ and $S_{r'}^-$ are spin raising and lowering operators on positions r and r' at time t and 0, respectively. The eigenvalue ω_q of the correlation function is the solution of the equation

$$\omega_q - \frac{J^2}{2} c_{Ru} \langle S_z \rangle \sum_p \frac{\langle c_{p\downarrow}^+ c_{p\downarrow}\rangle - \langle c_{p+q\uparrow}^+ c_{p+q\uparrow}\rangle}{\omega_q + \epsilon_{p+q} + U n_\downarrow - \epsilon_p - U n_\uparrow - J c_{Ru} S_z} - J\sigma_z = 0, \tag{5}$$

in which $\langle S_z \rangle$ and $\langle \sigma_z \rangle$ are the mean values of spin moments from the Ru ion and conducting electrons, respectively; $\langle c_{p+q\uparrow}^+ c_{p+q\uparrow}\rangle$ and $\langle c_{p\downarrow}^+ c_{p\downarrow}\rangle$ are electron densities with momentum $\vec{p}+\vec{q}$ and $\vec{p}$ with spins $\uparrow$ and $\downarrow$, and their corresponding kinetic energies are ϵ_{p+q} and ϵ_p, respectively; $n_\uparrow$ and $n_\downarrow$ are the mean values of up and down electron densities. It should be noted that Eq. (5) was derived from the mean-field scenarios for evaluating the magnetic moments and Coulomb interactions. It is worth mentioning that ω_q needs to be solved self-consistently because $\langle S_z \rangle$ is a function of ω_q and it can be obtained from Callen's formula [42], i.e.,

$$\langle S_z \rangle = \frac{[S-\Phi][1+\Phi]^{2S+1} + [S+1+\Phi][\Phi]^{2S+1}}{[1+\Phi]^{2S+1} - \Phi^{2S+1}}. \tag{6}$$

Φ is the magnon number, which has a relation with ω_Q by

$$\Phi(\omega_Q) = (1 + e^{\beta\omega_Q})^{-1}. \tag{7}$$

β is the inverse of temperature energy, i.e., $(k_B T)^{-1}$; S is the spin quantum number of the Ru ion. In stoichiometric $SrRuO_3$, S is +2, therefore the maximum $\langle S_z \rangle = 2$. Because of the considerable Ru vacancies in $SrRuO_3$, we suppose that S should be suppressed to lower than +2. For simplicity, we still set $\mathbf{S} = +2$ ignoring some low spin effects to S.

It is observed that with varying Coulombic energy, U, a finite magnon gap opens up at $Q = 0$, as shown in Fig. 3(b). Though the coupling does not follow the Heisenberg model, the dispersion curve near zone center can be approximated by the aforementioned quadratic equation with reliable accuracy.

IV. CONCLUSION

In summary, we have successfully measured the magnon dispersion curve of $SrRuO_3$ single crystal epitaxial film along the [002] direction by INS where the tiny material mass of the films is 0.9 mg. The present data reveals one significant

magnon dispersion curve along [002] following the quadratic ($E \propto Q^2$) relation, which shows a magnon gap of 0.32 meV. The near cubic structure suppresses the structural distortion and increases the isotropy. The higher symmetry and the impurity level, due to Ru and O vacancies, near Fermi level may possibly disrupt the spin-orbit coupling and the anticrossings and in turn could weaken or destroy the Weyl Fermion node and the magnon gap. In addition, the electrons captured by defects and site vacancies experiences on-site Coulomb interactions, which could resultantly open up a small magnon gap.

ACKNOWLEDGMENTS

The authors (H.C., S.J.S., and G.D.D) acknowledge the Ministry of Science and Technology (MOST), Taiwan for financial support through Grants No. MOST-108-2112-M-110-003, No. MOST-108-2911-I-390-501, and No. MOST-108-2811-M-110-509. Professor H. Chou (the major corresponding author) initiated the idea, planned all experiments and took part in all work. Dr. G. D. Dwivedi was responsible for film growth, XPS data analysis, and was involved in manuscript writing. Dr. C.-M. Wu was responsible for SIKA beam fine tuning and data collections. Professor J. W. Lynn, Dr. Guangyong Xu, Professor W. -H. Li, and Dr. C. H. Lee helped in taking data in SPINS and to confirm the data. B. Y. Chen helped in film growth. Dr. S. I. Yano assisted in understanding the strain effect. Professor S. J. Sun provided the crucial theoretical model to understand the suppression of the magnon gap. The authors extend their thanks to ANSTO and NIST for general assistance, to the Nano-center and Core-facilities centers of NSYSU for providing multiple instruments, such as XRD, TEM, AFM, and SQUID for characterizations. The authors also extend their gratitude to National Synchrotron Radiation Research Center (NSRRC), Taiwan for verifying the XPS data. The identification of any commercial product or trade name does not imply endorsement or recommendation by the NIST.

[1] J. J. Randall and R. Ward, J. Am. Chem. Soc. **81**, 2629 (1959).
[2] J. M. Longo, P. M. Raccah, and J. B. Goodenough, J. Appl. Phys. **39**, 1327 (1968).
[3] R. J. H. Voorhoeve, D. W. Jr. Johnson, J. P. Remeika, and P. K. Gallagher, Science **195**, 827 (1977).
[4] P. B. Allen, H. Berger, O. Chauvet, L. Forro, T. Jarlborg, A. Junod, B. Revaz, and G. Santi, Phys. Rev. B **53**, 4393 (1996).
[5] P. A. Joy, S. K. Date, and P. S. Anil Kumar, Phys. Rev. B **56**, 2324 (1997).
[6] G. Cao, S. McCall, M. Shepard, J. E. Crow, and R. P. Guertin, Phys. Rev. B **56**, 321 (1997).
[7] K. Yoshimura, T. Imai, T. Kiyama, K. R. Thurber, A. W. Hunt, and K. Kosuge, Phys. Rev. Lett. **83**, 4397 (1999).
[8] J. S. Ahn, J. Bak, H. S. Choi, T. W. Noh, J. E. Han, Y. Bang, J. H. Cho, and Q. X. Jia, Phys. Rev. Lett. **82**, 5321 (1999).
[9] B. Dabrowski, O. Chmaissem, P. W. Klamut, S. Kolesnik, M. Maxwell, J. Mais, Y. Ito, B. D. Armstrong, J. D. Jorgensen, and S. Short, Phys. Rev. B **70**, 014423 (2004).
[10] D. Popescu, B. Popescu, G. Jegert, S. Schmelzer, U. Boettger, and P. Lugli, IEEE Trans. Electron Devices **61**, 2130 (2014).
[11] M. Moors, K. K. Adepalli, Q. Lu, A. Wedig, C. Bäumer, K. Skaja, B. Arndt, H. L. Tuller, R. Dittmann, R. Waser, B. Yildiz, and I. Valov, ACS Nano **10**, 1481 (2016).
[12] C. Zhou, L. Wu, C. Zhang, J. Yao, and C. Jiang, J. Phys. D **49**, 425003 (2016).
[13] G. Herranz, B. Martinez, J. Fontcuberta, F. Sanchez, M. V. Garcia-Cuenca, C. Ferrater, and M. Varela, J. Appl. Phys. **93**, 8035 (2003).
[14] A. Vorobiev and S. Gevorgian, Appl. Phys. Lett. **104**, 222905 (2014).
[15] W. S. Chang, H. J. Liu, V. T. Tra, J. W. Chen, T. C. Wei, W. Y. Tzeng, Y. Zhu, H. H. Kuo, Y. H. Hsieh, J. C. Lin, Q. Zhan, C. W. Luo, J. Y. Lin, J. H. He, C. L. Wu, and Y. H. Chu, ACS Nano **8**, 6242 (2014).
[16] M. S. Anwar, S. R. Lee, R. Ishiguro, Y. Sugimoto, Y. Tano, S. J. Kang, Y. J. Shin, S. Yonezawa, D. Manske, H. Takayanagi, T. W. Noh, and Y. Maeno, Nat. Commun. **7**, 13220 (2016).
[17] L. Wang, Q. Feng, Y. Kim, R. Kim, K. H. Lee, S. D. Pollard, Y. J. Shin, H. Zhou, W. Peng, D. Lee, W. Meng, H. Yang, J. H. Han, M. Kim, Q. Lu, and T. W. Noh, Nat. Mater. **17**, 1087 (2018).
[18] M. Verissimo-Alves, P. García-Fernández, D. I. Bilc, P. Ghosez, and J. Junquera, Phys. Rev. Lett. **108**, 107003 (2012).
[19] F. Pulizzi, Nat. Mater. **11**, 564 (2012).
[20] J. M. Rondinelli, N. M. Caffrey, S. Sanvito, and N. A. Spaldin, Phys. Rev. B **78**, 155107 (2008).
[21] D. M. Paskiewicz, R. Sichel-Tissot, E. Karapetrova, L. Stan, and D. D. Fong, Nano Lett. **16**, 534 (2016).
[22] S. Kunkemöller, D. Brüning, A. Stunault, A. A. Nugroho, T. Lorenz, and M. Braden, Phys. Rev. B **96**, 220406(R) (2017).
[23] H. Mizuno, K. T. Yamada, D. Kan, T. Moriyama, Y. Shimakawa, and T. Ono, Phys. Rev. B **96**, 214422 (2017).
[24] G. Koster, L. Klein, W. Siemons, G. Rijnders, J. S. Dodge, C. B. Eom, D. H. A. Blank, and M. R. Beasley, Rev. Mod. Phys. **84**, 253 (2012).
[25] G. D. Dwivedi, S. J. Sun, Y. K. Kuo, and H. Chou, J. Phys.: Condens. Matter **31**, 125602 (2019).
[26] L. Klein, J. R. Reiner, T. H. Geballe, M. R. Beasley, and A. Kapitulnik, Phys. Rev. B **61**, R7842(R) (2000).
[27] F. Bern, M. Ziese, A. Setzer, E. Pippel, D. Hesse, and I. Vrejoiu, J. Phys.: Condens. Matter **25**, 496003 (2013).
[28] S. Itoh, Y. Endoh, T. Yokoo S. Ibuka, J. -G. Park, Y. Kaneko, K. S. Takahashi, Y. Tokura, and N. Nagaosa, Nat. Commun. **7**, 11788 (2016).
[29] K. Jenni, S. Kunkemöller, D. Brüning, T. Lorenz, Y. Sidis, A. Schneidewind, A. A. Nugroho, A. Rosch, D. I. Khomskii, and M. Braden, Phys. Rev. Lett. **123**, 017202 (2019).
[30] A. T. D. Grünwald, A. R. Wildes, W. Schmidt, E. V. Tartakovskaya, J. Kwo, C. Majkrzak, R. C. C. Ward, and A. Schreyer, Phys. Rev. B **82**, 014426 (2010).

[31] Murtaza Bohra, Kartikeya Negi, Varun Karthik Y. S., Hsiung Chou, X. Wang, and W. K. Chu, Sci. Rep. **7**, 4501 (2017).
[32] M. Bohra, C. P. Wu, H. J. Yeh, Y. H. Cheng, C. C. Peng, and H. Chou, J. Appl. Phys. **109**, 07D728 (2011).
[33] C. Sow, D. Samal, P. S. Anil Kumar, A. K. Bera, and S. M. Yusuf, Phys. Rev. B **85**, 224426 (2012).
[34] B. Dabrowski, S. Kolesnik, O. Chmaissem, T. Maxwell, J. Mais, and J. D. Jorgensen, Phys. Stat. Sol. B **243**, 13 (2006).
[35] R. Shimano, Y. Ikebe, K. S. Takahashi, M. Kawasaki, N. Nagaosa, and Y. Tokura, Euro. Phys. Lett. **95**, 17002 (2011).
[36] S. Lee, J. R. Zhang, S. Torii, S. Choi, D. -Y. Cho, T Kamiyama, J. Yu, K. A. McEwen, and J. -G. Park, J. Phys.: Condens. Matter **25**, 465601 (2013).
[37] L. Feng, T. Shiga, and J. Shiomi, Appl. Phys. Exp. **8**, 071501 (2015).
[38] C. Kittel, *Introduction to Solid State Physics* (Wiley, New York, 2005).
[39] M. C. Langner, C. L. S. Kantner, Y. H. Chu, L. M. Martin, P. Yu, J. Seidel, R. Ramesh, and J. Orenstein, Phys. Rev. Lett. **102**, 177601 (2009).
[40] S. J. Sun, H. Chou, and S. T. Lin, J. Phys.: Condens. Matter **31**, 275803 (2019).
[41] E. B. Guedes, M. Abbate, K. Ishigami, A. Fujimori, K. Yoshimatsu, H. Kumigashira, M. Oshima, F. C. Vicentin, P. T. Fonseca, and R. J. O. Mossanek, Phys. Rev. B **86**, 235127 (2012).
[42] Norberto Majlis, *The Quantum Theory of Magnetism* (World Scientific, Singapore, 2000), Chap. 5.